

Ultrafast electronic dynamics in polyatomic molecules studied using femtosecond vacuum ultraviolet and x-ray pulses

This content has been downloaded from IOPscience. Please scroll down to see the full text.

2014 J. Phys. B: At. Mol. Opt. Phys. 47 124001

(<http://iopscience.iop.org/0953-4075/47/12/124001>)

View [the table of contents for this issue](#), or go to the [journal homepage](#) for more

Download details:

IP Address: 130.54.110.71

This content was downloaded on 21/04/2015 at 02:51

Please note that [terms and conditions apply](#).

Review Article

Ultrafast electronic dynamics in polyatomic molecules studied using femtosecond vacuum ultraviolet and x-ray pulses

Toshinori Suzuki^{1,2,3}¹ Department of Chemistry, Graduate School of Science, Kyoto University, Kyoto 606-8502, Japan² Japan Science and Technology Agency, CREST, Sanbancho, Chiyoda-ku, Tokyo, 102-0075, Japan³ RIKEN Center for Advanced Photonics, RIKEN, Wako, Saitama 351-0198, JapanE-mail: suzuki@kuchem.kyoto-u.ac.jp

Received 24 December 2013

Accepted for publication 25 March 2014

Published 10 June 2014

Abstract

Time-resolved velocity map photoelectron imaging is performed using sub-20 fs deep ultraviolet and vacuum ultraviolet pulses to study electronic dynamics of isolated polyatomic molecules. The non-adiabatic dynamics of pyrazine, furan and carbon disulfide (CS₂) are described as examples. Also described is sub-picosecond time-resolved x-ray direct absorption spectroscopy using a hard x-ray free electron laser (SACLA) and a synchronous near ultraviolet laser to study ultrafast electronic dynamics in solutions.

Keywords: ultrafast, photoelectron, ultraviolet, x-ray, molecule

(Some figures may appear in colour only in the online journal)

1. Introduction

One of the keys for elucidating chemical reaction mechanisms is observation of ultrafast electronic dynamics driving nuclear motions in molecules. In these electronic dynamics, valence electrons play central roles, which are most clearly observed by ultrafast photoelectron spectroscopy using ultraviolet (UV) and vacuum ultraviolet (VUV) radiation. Inner-shell electrons usually play only minor roles; however, they exhibit characteristic chemical shifts of the electron binding energies, depending on oxidation states and chemical bonding of individual atoms. X-ray radiation is indispensable for observing these inner-shell electrons. Thus, ultrashort pulses from deep UV to x-ray are valuable tools to study electronic and chemical dynamics.

In the past decade, high harmonics generation (HHG) has opened new avenues to attosecond science and extreme UV (EUV) spectroscopy [1–3]. An HHG light source using a Ti:sapphire laser (800 nm) generates photon energies up to 100 eV, while an intense infrared driving laser can produce photons up to 1 keV. Compared to the third generation

synchrotron radiation facilities, HHG produces more than three orders of magnitude shorter pulse durations, enabling real-time observation of electronic dynamics. One of the difficulties in using HHG for EUV spectroscopy remains in the separation of single-order radiation from a comb-like structure of odd-order harmonics (or an extremely broad continuum), because multilayer mirrors with high reflectivity are only available for limited wavelength regions such as 6–7, 13.5 or 30 nm. New techniques such as the time-delay-compensated monochromator improve the efficiency and flexibility of wavelength separation. Thus, single-order high harmonics is becoming a more convenient EUV light source for spectroscopic purposes. Interested readers may refer to other articles in this special issue for details about the physics and applications of HHG.

One of the weak points of HHG is rather low pulse energy, typically tens of pJ after separation of a single order, although technical improvements are continuing to increase the pulse energy [4]. An alternative solution for generating intense VUV radiation is non-resonant four-wave mixing in filamentation propagation. Typical output pulse energies for

the input pulse energies of 0.5 mJ (770 nm) + 0.5 mJ (390 nm) are $>10 \mu\text{J}$ at 264 nm, $>1 \mu\text{J}$ at 198 nm, and $>100 \text{ nJ}$ at 159 nm [5–7]. Radiation at 130 nm has also been observed in our laboratory. The method only requires temporal and spatial overlap of intense femtosecond laser pulses in a rare gas cell. In the cell, the laser pulses alter the local refractive index of the gas and self-focus to cause ionization of the gas. Since the ionized gas species reverses the spatial gradient of the refractive index with respect to that of the neutral gas, the overall effect enables propagation of collimated laser beams over the Rayleigh length. Even if each of the two-colour laser pulses is not intense enough to create filamentation, cooperative interaction between the two-colour fields and the gas medium can induce filamentation propagation [6]. The intensity clamping and mode cleaning effects in filamentation provide stable and spatially clean output pulses [8].

While filamentation four-wave mixing is a table-top VUV light source, a free electron laser is a large-scale facility to generate ultrashort and ultraintense pulses from the VUV to hard x-ray region [9–12]. There are already a number of free electron lasers around the world, such as FLASH (free electron LASer in Hamburg), SCSS (Spring-8 Compact SASE source), LCLS (linac coherent light source), SACLA (Spring-8 Angstrom compact free electron LASer) and FERMI (free electron laser radiation for multidisciplinary investigation). (SASE stands for self-amplification of spontaneous emission.) SCSS is the first VUV free electron laser in Japan, and its central wavelength is 51–62 nm, although longer wavelengths can be generated under special operation conditions. The pulse energy from SCSS is as high as $30 \mu\text{J pulse}^{-1}$ at 60 nm, which is higher than that of HHG by orders of magnitudes. SACLA is a much larger facility with the total length of 700 m, and it is operated at a beam energy of 8.5 GeV. The photon energy range is 4.5–15 keV. When synchronized with a femtosecond laser, both SCSS and SACLA have timing jitter of several hundred femtoseconds, inherent to SASE. Picosecond time resolution can be obtained routinely, and subpicosecond time-resolution is obtainable using measurement of individual pulse timing. The severe limitations of free electron lasers based on using normal-conducting linear accelerators are low repetition rates (10–100 Hz) and difficulty to perform multiple experiments simultaneously, unlike synchrotron radiation facilities, owing to the nature of a linear accelerator. Various technical strategies, such as electron beam steering into multiple beam lines, are being planned to overcome these problems [13]. Yabashi *et al* reported more details about atomic, molecular and optical physics experiments at SCSS and SACLA [14].

In this article, I describe our recent experiments performed using VUV and x-ray radiation generated by filamentation four-wave mixing and SACLA, respectively. In section 2, I describe sub-20 fs pulse generation in the deep UV and VUV regions by multi-colour filamentation four-wave mixing. Time-resolved velocity map photoelectron imaging (TRPEI) of three molecules is discussed as applications of this light source. Pyrazine provides an example as to how the experimental study has progressed using both the filamentation light source and a free electron laser. Furan provides an example as to how theoretical simulation of TRPEI has

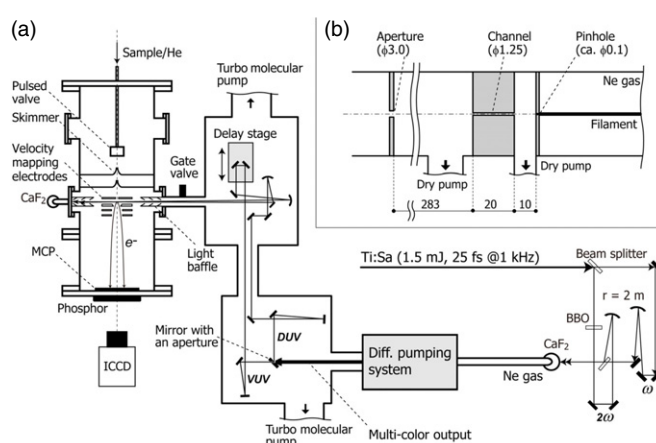


Figure 1. (a) Schematic diagram of our experimental setup for filamentation four-wave mixing. (b) Schematic drawing of the differential pumping system. All dimensions are given in millimeters. Reprinted with permission from [7]. © 2013 The Optical Society of America.

been improved to enable simulation of photoelectron angular distributions. CS₂ is the last example to show how a VUV probe pulse captures the entire wave packet motions in the excited state. In section 3, I discuss pump–probe x-ray absorption spectroscopy using SACLA and a synchronous femtosecond laser to study electronic dynamics in solution, in which a dispersive spectrometer and a dual beam method are employed [15]. Section 4 provides a summary and outlook.

2. Sub-20 fs time-resolved velocity map photoelectron imaging

2.1. Generation of multicolour sub-20 fs pulses by filamentation four-wave mixing

Filamentation four-wave mixing enables generation of ultrashort pulses in the deep UV and VUV regions simultaneously in a single rare gas cell. This single cell scheme provides a simple optical setup with very precise and stable optical pump–probe delay. The generation scheme of the multiple colours is cascaded four-wave mixing processes. In our initial study [5], we demonstrated simultaneous generation of only the third and fourth harmonics (3ω and 4ω , respectively). Although the fifth and sixth harmonics (5ω and 6ω) must have been generated, the optical path was in air and not transparent to VUV radiation. Our current experimental setup has the entire optical paths under vacuum from the filamentation cell to the target to use VUV radiation [7].

Figure 1(a) shows a schematic diagram of our apparatus. A cryogenically cooled Ti:sapphire multipass amplifier delivers $\sim 770 \text{ nm}$ pulses (25 fs, 1.5 mJ) at 1 kHz. The fundamental frequency pulse (ω) is split into two beams with a ratio of 3:7. The higher intensity beam is converted to the second harmonic, 2ω , in a β -barium borate crystal (β -BBO, $\theta = 29^\circ$, $t = 0.3 \text{ mm}$). A dielectric concave mirror ($r = 2,000 \text{ mm}$) focuses the second harmonic into a neon gas cell through a Brewster-angled calcium fluoride (CaF₂) window ($t = 1 \text{ mm}$). This concave mirror also separates the second harmonic from the

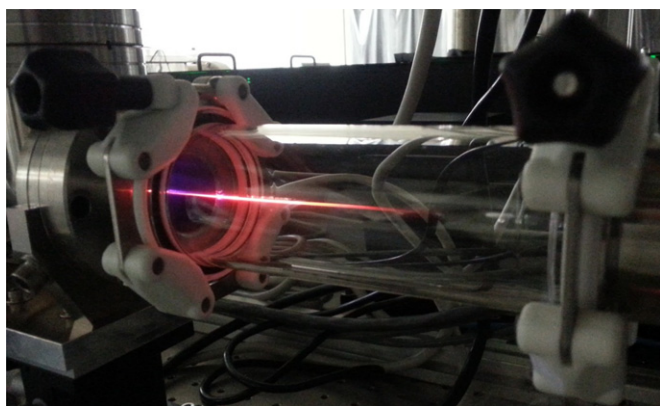


Figure 2. Photograph of filamentation in Ne gas.

residual fundamental. The fundamental beam is focused into the cell with another dielectric concave mirror ($r = 2,000$ mm). A flat dichroic mirror is used to recombine the fundamental and second harmonic beams. The relative polarization of two beams is parallel to each other. The pulse energies of the fundamental and the second harmonic are 0.43 and 0.37 mJ, respectively. When the ω and 2ω pulses overlap temporally and spatially, a bright filament (plasma column) with the length of ca. 120 mm is created (figure 2).

For obtaining VUV radiation from the filamentation cell, one may use an optical window such as MgF_2 . Then, dispersion caused by the output window must be compensated, for example, by chirping one of the input pulses [16]; however, it transfers only the even orders of spectral chirp to the four-wave mixing pulse, so that dispersion cannot be perfectly compensated. Alternatively, we avoid material dispersion simply by eliminating transmissive optics in the paths after the four-wave mixing. A pinhole is employed, instead of an output window, for the filamentation cell to transmit the deep UV and VUV pulses generated by four-wave mixing. The neon gas leaking through the pinhole is evacuated with a dry pump (580 L min^{-1}). As shown in figure 1(b), a narrow channel (1.25 mm in diameter and 20 mm in length) and an aperture (3 mm ϕ) are placed behind the pinhole to minimize conductance and improve differential pumping. The pressure of neon gas in the gas cell is $\sim 3.7 \times 10^2$ Torr. The pressure in this first differential pumping section is below 3.0×10^{-1} Torr. The region between the channel and the aperture is evacuated with another dry pump (500 L min^{-1}). The flow rate of neon gas is $0.5 \text{ Torr} \cdot \text{L s}^{-1}$.

The laser pulses finally enter a high-vacuum optics chamber that houses an optical delay stage and mirrors. A UV-enhanced aluminium mirror with an aperture of 3 mm diameter is used to spatially separate the central and peripheral parts of the beam. The central part is transmitted through this holed mirror and reflected five times with dielectric mirrors for 5ω in order to attenuate other colours (ω , 2ω , 3ω and 4ω). The peripheral part reflected by the holed mirror is used to sample 3ω or 4ω , using dichroic mirrors. The timing of the 5ω pulse is varied using a vacuum-compatible translational stage with 5 nm resolution. The VUV and deep UV pulses are independently focused onto a molecular beam with two Al concave mirrors ($r = 1000$ mm). The intersection angle

between the VUV and deep UV pulses is ca. 1° . The entire optics chamber is evacuated using two turbo molecular pumps (300 L s^{-1}) to maintain the pressure below 2×10^{-6} Torr when operating the filamentation gas cell. The spectra of 3ω , 4ω , and 5ω pulses generated by cascaded four-wave mixing are shown in figure 3. The transform-limited pulse widths are estimated as 9, 7, and 6 fs for 3ω , 4ω , and 5ω , respectively.

The photoelectron velocity map imaging apparatus [17, 18] with a doubly-skimmed molecular beam source is employed with a pulsed gas valve [19]. Photoelectrons generated by $(1 + 1')$ resonantly enhanced two-photon ionization of jet-cooled samples are accelerated in an electric field and projected onto a dual microchannel plate (effective area of 75 mm ϕ) backed by a phosphor screen (P46). The linear polarization vectors of the VUV and deep UV pulses are aligned parallel to each other and also set parallel to the microchannel plate detector face. Photoelectron images are recorded as a function of the delay time between deep UV and VUV pulses and analysed by the pBASEX method [20] to obtain time-dependent photoelectron kinetic energy and angular distributions.

The cross-correlation trace between 4ω and 5ω measured using non-resonant $(1 + 1')$ two-photon ionization of Xe is shown in figure 4. The background signal (~ 640) originates from two-photon ionization by individual one-colour ionization processes. As shown in figure 3, the observed trace is well expressed by a single Gaussian with a full width at half maximum of 17 ± 2 fs (a solid line); which suggests that the individual pulses of 4ω and 5ω have pulse durations of about 12 fs.

The $\omega + 2\omega$ is not the only method for generation of 5ω . Zuo *et al* employed the $2\omega + 3\omega$ scheme to generate 4ω and 5ω simultaneously [16, 21]. If only 5ω is necessary, one can also employ the $\omega + 3\omega$ scheme. With the latter, Ghotbi *et al* demonstrated generation of $2.5 \mu\text{J pulse}^{-1}$ radiation at 160 nm using noncollinear geometry for four-wave mixing [22]. Beutler *et al* have employed a tandem filamentation cell to compress ω and perform the $\omega + 3\omega$ scheme to generate a 16.4 fs pulse at 160 nm [23].

2.2. Photoelectron imaging of S_2 - S_1 internal conversion in pyrazine

The $S_2(^1B_{2u}, \pi\pi^*)$ - $S_1(^1B_{3u}, n\pi^*)$ internal conversion of pyrazine ($\text{C}_4\text{H}_4\text{N}_2$, D_{2h}) is one of the best-known examples of ultrafast electronic deactivation via a conical intersection [24]. The topography of this conical intersection has been extensively studied by *ab initio* molecular orbital calculations (see [25] and references therein). Although pyrazine has 24 normal modes, only a single mode, $Q_{10a}(b_{1g})$, mediates S_2 - S_1 coupling due to the selection rule. Furthermore, only a few totally symmetric (a_g) modes participate in the short-time vibrational dynamics of this system. This reduced dimensionality makes pyrazine a benchmark for theoretical studies of ultrafast internal conversion via a conical intersection. However, real-time observation of this process was not possible owing to the lack of a suitable ultrafast laser in the deep UV region.

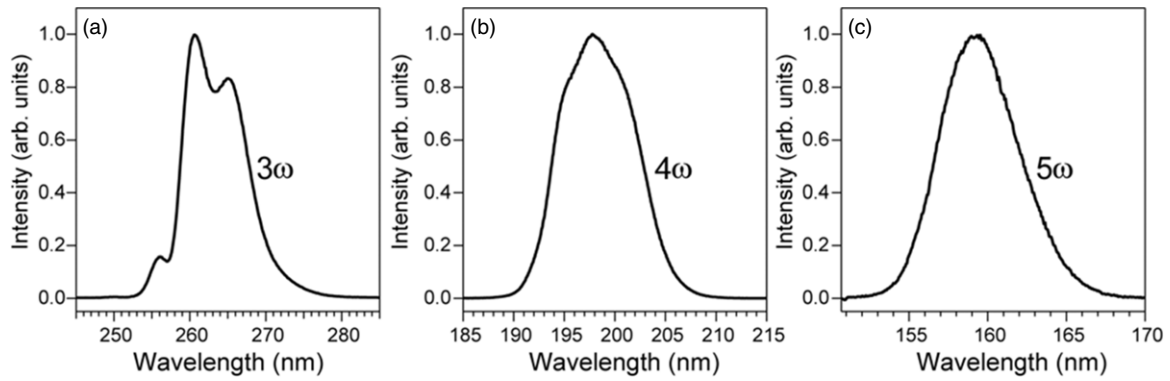


Figure 3. Typical spectra (a) 3ω , (b) 4ω , and (c) 5ω . Reprinted with permission from [7]. © 2013 The Optical Society of America.

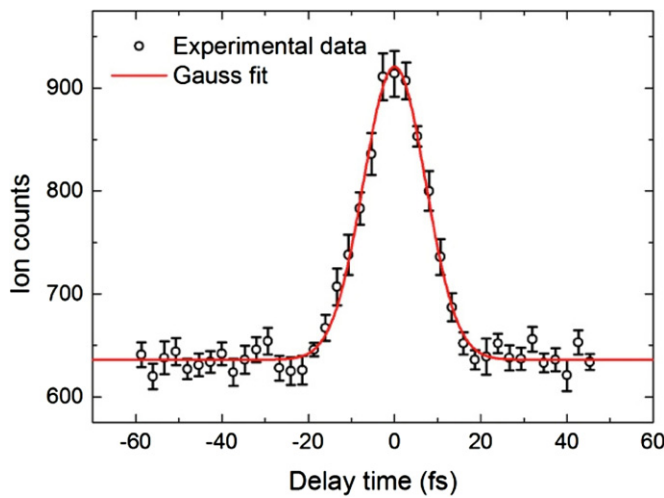


Figure 4. Cross-correlation trace between 4ω and 5ω pulses measured by non-resonant two-photon ionization of an atomic beam of Xe.

Figure 5(a) shows the UV photoabsorption spectra of pyrazine (pyrazine-h4) and fully deuterated pyrazine (pyrazine-d4) vapour measured at room temperature. Overlaid are the spectra of our pump (264 nm: blue) and probe (198 nm: red) pulses. The pump pulse overlaps with the S_2 – S_0 band near the origin, while the probe pulse overlaps (unfavourably) with the S_3 – S_0 band slightly. Figure 5(b) shows a schematic energy diagram of our experiment. The sum of the photon energies of the pump (4.70 eV) and probe (6.26 eV) pulses is 10.96 eV, which enables ionization to the three ion states of D_0 , D_1 , and D_2 energetically.

The photoelectron kinetic energy and angular distribution in $(1 + 1')$ photoionization is expressed as follows (the prime means different colour):

$$I(t, E, \theta) = \frac{\sigma(t, E)}{4\pi} \{1 + \beta_2(t, E)P_2(\cos \theta) + \beta_4(t, E)P_4(\cos \theta)\} \quad (1)$$

where t , E , θ , and are the pump–probe time delay, the photoelectron kinetic energy and the electron ejection angle from the laser polarization direction. $P_n(x)$ are the n th order Legendre polynomials. $\sigma(t, E)$ represents a photoelectron kinetic energy distribution (photoelectron spectrum). $\beta_2(t, E)$ and $\beta_4(t, E)$ are called anisotropy parameters. The three scalar quantities of $\sigma(t, E)$, $\beta_2(t, E)$ and $\beta_4(t, E)$ in equation (1) are the

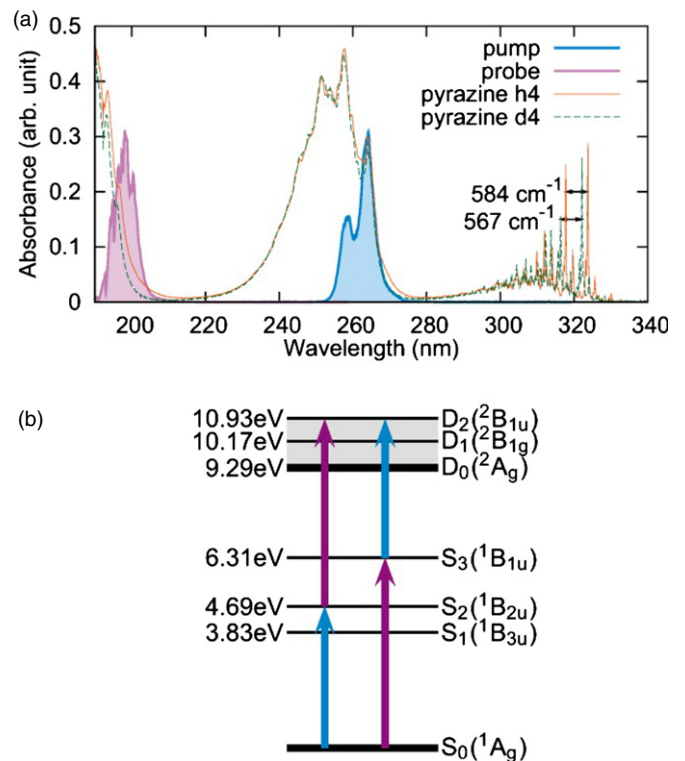


Figure 5. UV photoabsorption spectra of (a) S_1 , S_2 , and S_3 of pyrazine-h4 (orange solid line) and pyrazine-d4 (green dashed line) at room temperature. The spectra of our pump (264 nm, 4.70 eV) and probe (198 nm, 6.26 eV) pulses are also shown in blue and violet. (b) Schematic energy diagram of pyrazine. Reprinted with permission from [26]. © 2010 American Institute of Physics.

observables in $(1 + 1')$ TRPEI (time-resolved photoelectron imaging). Extraction of dynamical information from $\beta_2(t, E)$ and $\beta_4(t, E)$ is the heart of TRPEI.

Figure 6 presents the experimental results of TRPEI of pyrazine [25, 27, 28]. Figure 6(b) shows the total photoelectron signal as a function of the pump–probe time delay. Since the spectra of our pump and probe pulses overlap the S_2 – S_0 and S_3 – S_0 bands, respectively, the 264 nm pulse excites ground-state molecules to S_2 and the 198 nm pulse ionizes them for a positive time delay, while for a negative time delay, the roles of the 198 nm and 264 nm pulses are interchanged and molecules are ionized from S_3 . The signal at a positive time delay rapidly decays in less than 30 fs and exhibits a plateau; this

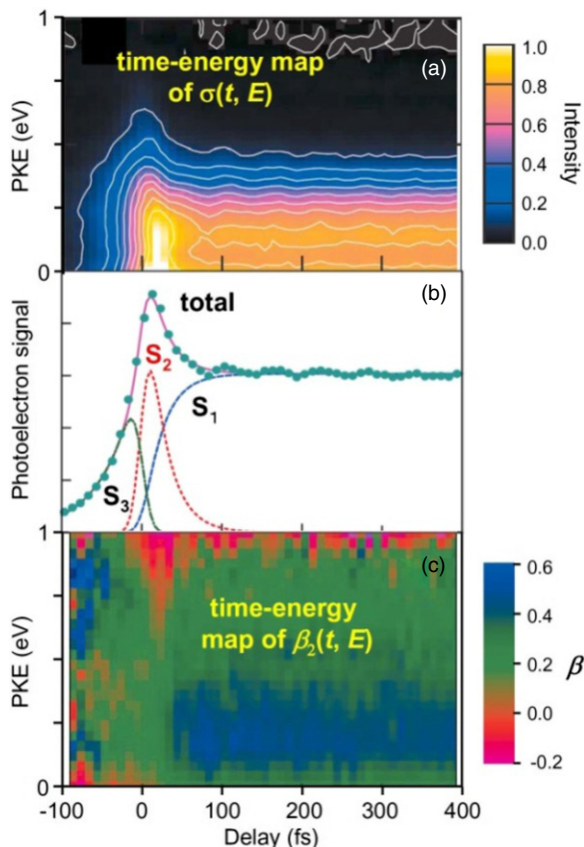


Figure 6. (a) Time-evolution of the photoelectron kinetic energy distribution, $\sigma(t, E)$. (b) Temporal profiles of the total photoelectron signals in $(1+1')$ TRPEI of pyrazine-h4. The observed data are well explained by three components: single-exponential decay of S_2 (red), corresponding increase in S_1 (blue) at a positive time delay, and single-exponential decay of S_3 (green) at a negative time delay. The fitting result is shown by the solid line. (c) Time-evolution of photoelectron angular anisotropy parameter $\beta_2(t, E)$.

plateau has a finite lifetime of 22 ps for pyrazine-h4 [29, 30]. Furthermore, the plateau region exhibits oscillatory features due to vibrational quantum beats. The Fourier transform of the oscillation ($t > 50$ fs) exhibits a frequency component of $560 \pm 40 \text{ cm}^{-1}$, which agrees with the vibrational frequency of Q_{6a} in S_1 (583 cm^{-1}). In the negative time range, the signal diminishes very rapidly within 100 fs (towards the $-\infty$ direction). The observed profile can thus be explained by three components: the decay of optically excited S_2 , the corresponding growth of S_1 populated by internal conversion from S_2 , and the decay of S_3 . By least-squares fitting, the $S_2 \rightarrow S_1$ internal conversion time constants are estimated to be 23 ± 4 fs. The $\sigma(t, E)$ shown in figure 6(a), does not exhibit any marked change on $S_2 \rightarrow S_1$ internal conversion. This is because photoionization occurs predominantly as $D_0(n^{-1}) \leftarrow S_1(n, \pi^*)$ and $D_1(\pi^{-1}) \leftarrow S_2(\pi, \pi^*)$, and the energy gaps between D_1 and D_0 (0.88 eV) and between S_2 and S_1 (0.86 eV) are almost the same.

Figure 6(c) shows a time–energy map of $\beta_2(t, E)$. The positive (blue–green) and negative (red) values correspond to preferential ejection of an electron parallel and perpendicular to the probe laser polarization [see equation (1)]. The energy dependence of β_2 , a coloured stripe at each time delay in

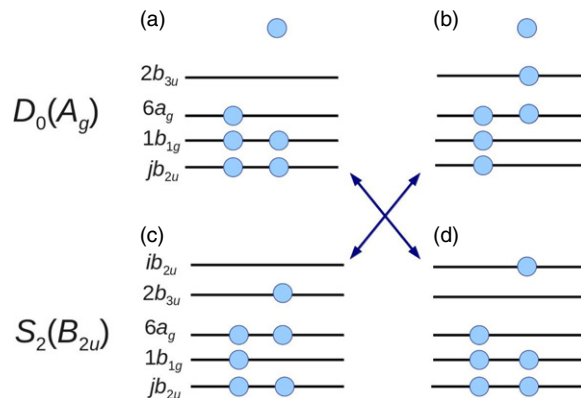


Figure 7. Electronic configurations of D_0 and S_2 . The leading configurations of D_0 and S_2 are shown in (a) and (c), respectively. By two-electron excitation, configurations (b) and (d) are obtained from configurations (a) and (c), respectively. Arrows indicate the allowed transition by one-photon ionization. Filled circles represent electrons. Isolated electrons at the top of panels (a) and (b) represent photoelectrons.

figure 5(b), is a fingerprint of the electronic character. The time–energy map clearly shows that there are three different components, one at a negative time delay and two at a positive time delay, which agrees with the analysis of $\sigma(t, E)$. The most distinctive feature is the sudden change in the colour at ca. 30 fs, which is attributed to ultrafast $S_2 \rightarrow S_1$ internal conversion. $\beta_2(t, E)$ does not change after 30 fs, indicating that the (n, π^*) electronic character remains; no restoration of the (π, π^*) character is identified. This lack of recurrence is possibly related to the photoexcitation energy; we excited pyrazine near the S_2 origin. Consequently, if the vibrational energy flows into various modes in S_1 , the wave packet has no chance to return to the Franck–Condon region in S_2 .

Within the lifetime (22 fs) of the S_2 state, a PKE > 0.8 eV is created by $D_0 \leftarrow S_2$. However, this ionization process is forbidden for the main electron configurations of D_0 and S_2 ; therefore, the occurrence of this process indicates that D_0 and S_2 consist of multiple electron configurations. The D_0 configurations that can be created by one-photon ionization from S_2 are those obtained by removing one electron from an orbital (ϕ) of the S_2 configuration, i.e.,

$$\psi(S_2) = \psi(D_0) \times \phi, \quad (2)$$

where $\Psi(S_2)$ and $\Psi(D_0)$ respectively denote the electron configurations of S_2 and D_0 . Because $\Psi(D_0) \times \phi$ should have the same symmetry species as S_2 [$\Gamma(S_2) = \Gamma(D_0) \times \Gamma(\phi)$], ϕ must be the b_{2u} orbital as given by the direct product $A_g(D_0) \times B_{2u}(S_2)$. However, no b_{2u} orbital exists among the outer valence and π^* orbitals, which implies that $D_0 \leftarrow S_2$ cannot be well described by typical valence complete active space self-consistent field (CASSCF) wavefunctions. To make the calculations tractable, we focused on configurations that are doubly excited with respect to the main configuration [28]. Figure 7 shows examples of such configurations. The configurations shown in figures 7(b) and (d) can be obtained by two-electron excitations from the D_0 and S_2 main configurations shown in figures 7(a) and (c), respectively. Ionization from the configuration in figure 7(d) to that in 7(a)

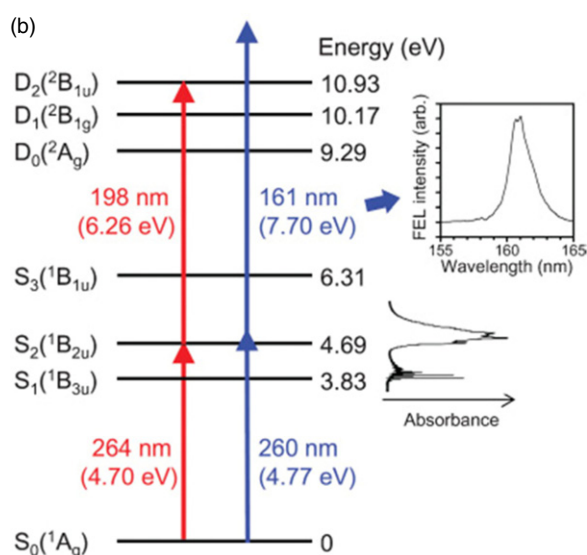
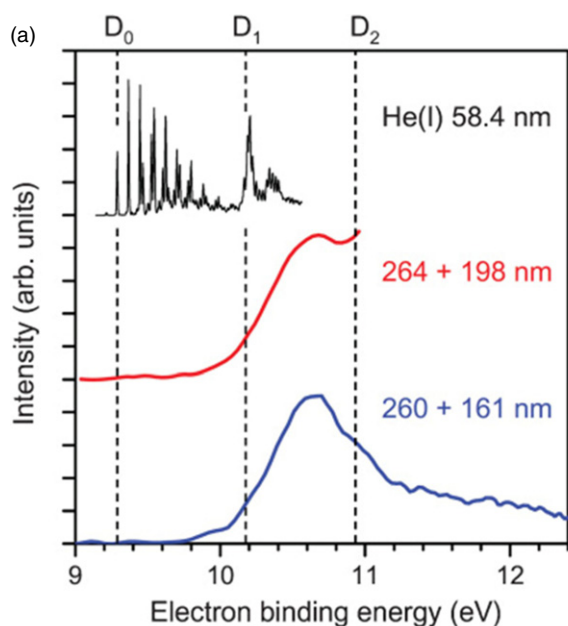


Figure 8. (a) PKED in He(I) photoelectron spectroscopy of ground-state pyrazine (black), 264 nm pump and 198 nm probe experiment (red) and 260 nm pump and 161 nm probe (blue). (b) Schematic energy diagram of the ionization process. Insets show the UV absorption spectrum of pyrazine vapour at room temperature and a time-averaged spectrum of SCSS. Reprinted with permission from [31]. © 2010 American Physical Society.

and from the configuration in figures 7(c) to 7(b) is possible. Including these configurations, the first-order configuration interaction calculations account for all one-electron excitations from the complete active space of eight orbitals. From our calculations, we find the contributions to the spectral intensity [42] of 47% from $3b_{2u}$, 27% from $4b_{2u}$, and 26% from all virtual b_{2u} (jb_{2u} , $j \geq 5$) [28]. This result clearly demonstrates that the electron correlation cannot be neglected for either D_0 or S_2 .

The $\sigma(t, E)$ shown in figure 6(a) exhibits non-zero intensity down to 0 eV. This clearly demonstrates that the Franck–Condon envelopes are not fully covered for photoionization from S_2 and S_1 due to the probe photon energy

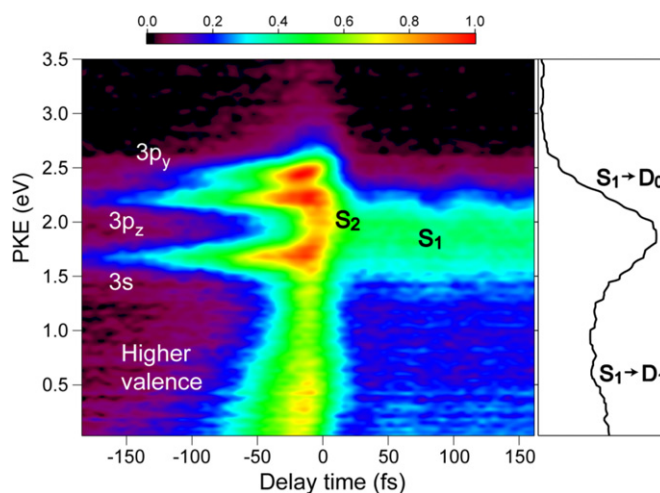


Figure 9. Photoelectron kinetic energy distribution observed for pyrazine using 264 nm pump and 159 nm probe pulses. Negative delay times indicate that the probe pulse precedes the pump pulse. The panel on the right shows the distribution integrated for the time delay of 50–150 fs.

being too low. Thus, we also performed TRPEI experiments using VUV radiation from SCSS as a probe pulse [31]. Figure 8 compares the photoelectron spectrum measured using the probe pulses of 161 nm radiation from SCSS and the 198 nm radiation from our filamentation four-wave mixing light source in the laboratory [31]. The former distribution exhibits a maximum in the region ca. 1.2 eV above D_0 , which is consistent with the vibrational energy of ca. 0.9 eV in S_1 . Since S_1 is the (n, π^*) state and D_0 and D_1 are n^{-1} and π^{-1} states, the frozen-core approximation predicts ionization occurs from S_1 to D_0 , as discussed earlier. On the other hand, since SCSS uses SASE, the timing jitter between the SCSS and a femtosecond laser is of the order of sub-picoseconds, which did not enable us to observe S_2 – S_1 ultrafast internal conversion in pyrazine in real time. Therefore, we generated VUV radiation (159 nm) using filamentation four-wave mixing and revisited this problem.

Figure 9 shows the time–energy map of the photoelectron energy distribution observed using the filamentation light source. In the negative time range, three Rydberg states of $3s$, $3p_y$ and $3p_z$ exhibit sharp horizontal distributions and a valence state exhibits a distribution that diminishes the kinetic energy rapidly and disappears within 100 fs. In the positive time range, the photoionization from S_2 and S_1 are observed, although the signal around $t = 0$ is rather congested due to both the 264 nm pump and 159 nm pump signals. The photoelectron kinetic energy distribution after the pump–probe delay of 100 fs is essentially the same as that obtained using SCSS. More detailed accounts of these results are presented elsewhere.

2.3. Photoelectron imaging of internal conversion in furan

Furan (C_4H_4O , C_{2v}) exhibits a broad UV absorption spectrum that has been ascribed to four electronic transitions to the ${}^1A_2(\pi, 3s)$, ${}^1B_2(\pi, \pi^*)$, ${}^1A_1(\pi, \pi^*)$, and ${}^1B_1(\pi, 3p_y)$ states, in which the transition to 1A_2 is weakly allowed by vibronic

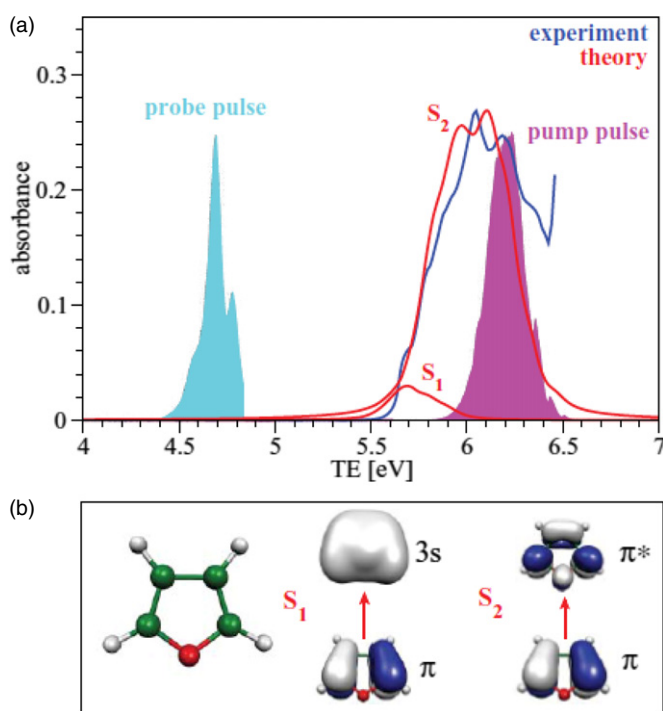


Figure 10. (a) Absorption spectrum (blue) of furan at room temperature and theoretical spectrum (red) for $S_1(^1A_2(\pi, 3s))$ and $S_2(^1B_2(\pi, \pi^*))$ states at $T = 300$ K. The discrete absorption lines for each member of the ensemble were convoluted with a Lorentzian function with a width of 0.1 eV and added together. The spectra of our pump (6.2 eV, 200 nm) and probe (4.7 eV, 260 nm) pulses are shown as filled curves. (b) Equilibrium structure of furan in the neutral ground state with character of the $S_1(\pi, 3s)$ and $S_2(\pi, \pi^*)$ transitions. Reprinted with permission from [26]. © 2010 American Institute of Physics.

coupling with 1B_2 . Figure 10 shows the absorption spectrum at room temperature and the corresponding theoretical spectrum calculated by time-dependent density functional theory [13]. The strong absorption feature at ~ 6 eV is due to the $S_2 \leftarrow S_0$ transition, and the weak feature in the low energy part (5.6–6.0 eV) corresponds to the $S_1 \leftarrow S_0$ transition. Another strong transition of $^1B_1(\pi, 3p_y) \leftarrow S_0$ is at 6.45 eV and outside of our pump spectrum.

The observed time profiles of photoion and photoelectron signals are shown in figure 11(a). The least-squares fitting assuming a single exponential function (green solid line in figure 11(a)) provides the lifetime of the excited state as 46 fs; the single exponential decay, however, does not provide an adequate fit of the time profile. For comparison, a time profile extracted for the specific kinetic energy of 1.6 eV is well reproduced by a single exponential function, as shown in a solid line in figure 11(b). The signal in figure 11(b) appears immediately at the time origin, indicating that this state is directly photoexcited from S_0 ; the lifetime of this state is 29 fs.

The experimental time–energy maps of $\sigma(t, E)$ and $\beta_2(t, E)$ are respectively shown in figures 12(b) and 13(b) [32]. Each map can be separated into regions of $E > 1.5$ eV (region A) and 0.0–1.5 eV (region B). The former exhibits high β_2 values (~ 0.8) that are typical of photoionization from a 3s Rydberg state. The kinetic energy of 1.6 eV is smaller by

0.4 eV than the maximum possible energy of 2.0 eV, which is consistent with the estimated vibrational energy in S_1 , ca. 0.3–0.4 eV. The region B exhibits a broad $\sigma(t, E)$ and low β_2 , which indicates ionization from a valence state $^1B_2(\pi, \pi^*)$. The intensity maxima of $\sigma(t, E)$ in region B are systematically time-delayed for lower energy. The lag time is ascribed to vibrational wave packet motion from the Franck–Condon region to the molecular structure monitored with a particular photoelectron kinetic energy. The results suggest that the molecules photoexcited to $^1B_2(\pi, \pi^*)$ undergo large structural deformation within 50 fs, and that they do not undergo efficient internal conversion to $^1A_2(\pi, 3s)$, contradicting with the theoretical prediction previously made [33, 34].

Theoretical simulation of TRPEI of polyatomic molecules is a highly challenging task. One difficulty arises from the fact that a polyatomic molecule has a number of vibrational degrees of freedom, for which accurate calculations of the potential energy surfaces and propagation of nuclear wave packet are computationally highly demanding. Calculations with reduced vibrational dimensionality are not desirable, because the photoionization Franck–Condon factor has to be taken into account for all vibrational degrees of freedom even if ultrafast dynamics in the excited electronic state(s) occur within limited vibrational degrees of freedom. This is clear when a large geometrical change occurs between the neutral and cationic states. Another difficulty arises in the theoretical description of ionization continua and calculations of transition dipole moments for bound–free photoionization. As our experimental study on pyrazine [25] has demonstrated clearly, the photoelectron angular distribution can reveal an abrupt change of electronic character upon a non-adiabatic transition, so that the theoretical model should be able to simulate the photoelectron angular anisotropy. One of the methods to obtain the photoionization transition dipole moments is Schwinger variational calculations [35]. Arasaki *et al* have performed such calculations on TRPEI of the excited state dynamics of NO_2 [36].

The photophysics of furan has been previously studied by multiconfigurational time-dependent Hartree wavepacket calculations with the potential energy surfaces determined by the *ab initio* equation-of-motion coupled cluster method [34]. The calculations predict that the $^1B_2(\pi, \pi^*)$ state undergoes ultrafast internal conversion to $^1A_2(\pi, 3s)$ within ~ 25 fs through a conical intersection, while the lifetime of $^1A_2(\pi, 3s)$ is longer than 200 fs. The conical intersection with S_0 , however, was not considered in these calculations. Another theoretical study, using a combined density functional/multireference configuration interaction method, suggested that molecules excited to the $^1B_2(\pi, \pi^*)$ state undergo a ring-opening reaction via the $^1B_1(\pi, \sigma^*)$ state [37]. We have simulated the TRPEI of furan using molecular dynamics (MD) on the fly in the frame of TDDFT and assuming constant photoionization transition dipole moments to the D_0 state [26]; MD on the fly is a method that calculates classical trajectories for all vibrational coordinates using the forces given by TDDFT. The simulations have reproduced the experimental photoelectron kinetic energy spectra; however, the method did not enable calculations of the photoelectron

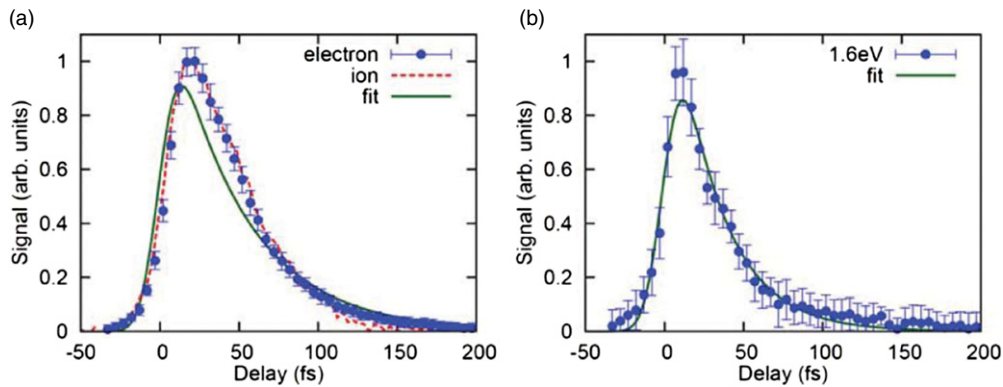


Figure 11. (a) Temporal profiles of total photoelectron (solid circles) and photoion (dotted line) signal in $(1 + 1')$ TRPEI of furan. The result of least-squares fitting with a single exponential decay $[\exp(-t/\tau)]$ convoluted with our apparatus function (Gaussian with 22 fs FWHM) is also shown as a solid line ($\tau = 46.3$ fs). (b) Temporal profile of photoelectron intensity at a photoelectron kinetic energy of 1.6 eV. The result of least-square fitting with a single exponential decay convoluted with the apparatus function is shown as a solid line ($\tau = 29.0$ fs). Reprinted with permission from [26]. © 2010 American Institute of Physics.

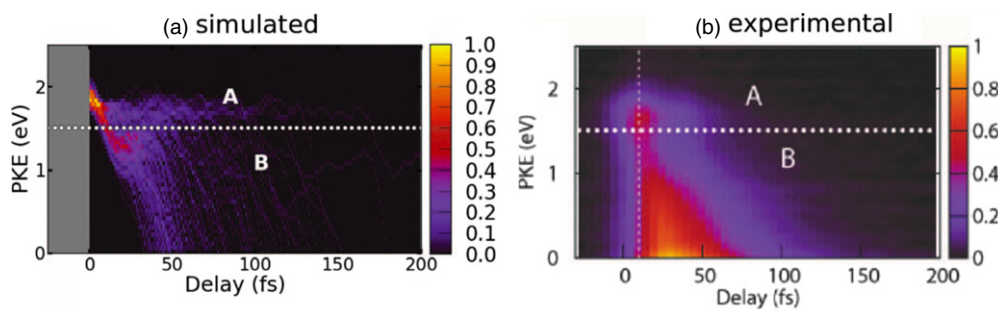


Figure 12. (a) Calculated photoelectron kinetic energy (PKE) distribution $\sigma(t, E)$ for 198 nm photoexcitation and 264 nm photoionization of furan. (b) Experimentally observed $\sigma(t, E)$. The vertical dotted line is at a delay time of 10 fs, where the temporal peaks of high-energy components appear. The high and low energy components, separated by horizontal lines, were denoted by A and B, respectively. Reprinted with permission from [32]. © 2013 American Institute of Physics.

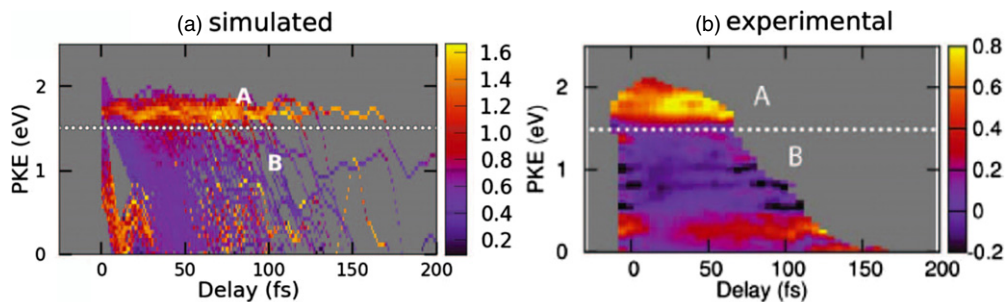


Figure 13. (a) Calculated values of the time-dependent photoelectron anisotropy parameter $\beta_2(t, E)$ for furan. The high and low energy components, separated by horizontal lines, were denoted by A and B, respectively. (b) $\beta_2(t, E)$ extracted from observed photoelectron images of furan. Reprinted with permission from [32]. © 2013 American Institute of Physics.

angular anisotropies. Therefore, Mitric and coworkers have improved the description of the ionization process using the Dyson orbital for the ionized orbital and atomic partial waves in a pure Coulombic potential for the photoelectron wave function [32]. The Dyson orbital is a single electron wave function defined as the overlap between the neutral electronic state with N electrons and the cationic state with $N-1$ electrons, and it facilitates a simple and reasonably accurate description of the photoionization step. Approximation of a photoelectron wavefunction using partial waves in a pure Coulombic potential ignores the dynamical phase shifts of the partial waves and shape resonances. The accuracies of these

approximations need to be tested against experimental results on various systems.

Figure 12 compares (a) the theoretical simulation by Mitric and coworkers and (b) the experimental result [32]. The theoretical simulation well reproduces formation of the $3s$ Rydberg state in the energy region indicated as A and rapid motion of the wave packet across region B within 50 fs. A more impressive agreement with the experiment is the time-energy map of anisotropy parameter shown in figure 13. Note that the absolute magnitudes of the anisotropy parameters are different between the theoretical and experimental results. However, the general trends are in good agreement. First of

all, high anisotropy observed for the 3s Rydberg state in region A is well reproduced in the calculation. Lower anisotropies in region B are also found in both the calculation and experiment. The high anisotropy experimentally observed at around 0.2–0.3 eV is due to ionization to the D_1 state of furan; however, when a major component of D_0 – S_2 produces photoelectrons in the same energy region at around a time delay of 20–30 fs, it dominates and reduces the anisotropy suddenly. The calculation captures this sudden drop of the photoelectron anisotropy. Thus, comparison with our experiment reveals that calculations based on the crude approximations using the Dyson orbital and atomic partial waves in Coulombic potential still provide useful theoretical support to experiments.

2.4. Photoelectron imaging of ultrafast dynamics in CS_2

CS_2 is linear in the electronic ground state ($^1\Sigma_g^+$), while photoexcitation in the wavelength region of 192–208 nm promotes a molecule to $^1B_2(^1\Sigma_u^+)$ with a quasi-linear structure. This photoexcitation induces symmetric stretching ($\nu_1 = 392\text{ cm}^{-1}$) and bending ($\nu_2 = 426\text{ cm}^{-1}$) vibrations. At 198 nm, the molecule is above the barrier for linearity, so that a large amplitude vibration occurs in the bending mode between the linear and bent geometries. Although the $^1B_2(^1\Sigma_u^+)$ state is bound in the linear geometry, it undergoes avoided crossings with the repulsive $^1B_2(^1\Pi_g)$ state at large bending angles, so that the molecule predissociates into $CS(^1\Sigma^+) + S(^1D)$ and $CS(^1\Sigma^+) + S(^3P)$. The photodissociation dynamics of CS_2 have been studied by a number of researchers, while ultrafast spectroscopy has been limited [38–44].

Farmanara *et al* studied the ultrafast excited state dynamics of CS_2 in the $^1B_2(^1\Sigma_u^+)$ state using a 201.4 nm pump pulse and a 268 nm probe pulse in 1999; the pulse duration was ca. 130 fs [38]. The observed transient ion signal was approximated as a single exponential decay associated by a vibrational quantum beat. The time-resolved photoelectron spectra of CS_2 was observed in 2006 by Townsend *et al* using a 201.3 nm pump and a 268 nm probe pulses [40]. Essentially the same yet more detailed spectra was also reported by Bisgaard *et al* in 2009; furthermore, Bisgaard *et al* aligned CS_2 by non-resonant rotational excitation using an 805 nm pulse prior to performing pump–probe photoelectron spectroscopy and measured the photoelectron angular distribution for the aligned ensemble of molecules [41]. Hockett *et al* have presented detailed accounts on these time-dependent photoelectron angular distributions [43]. Fuji *et al* have applied sub-20 fs deep UV pulses (198 and 264 nm) generated by filamentation four-wave mixing to the excited state dynamics of CS_2 in 2011; the cross-correlation was 22 fs [44]. With a considerably higher time resolution, the transient photoelectron spectra exhibited very clear wave packet motion in the $^1B_2(^1\Sigma_u^+)$ state. All of these previous studies [38–44] employed the third harmonic of the Ti:sapphire laser as the probe pulse; however, the probe photon energy was insufficient for observing the entire wave packet dynamics on the excited state potential energy surfaces.

Horio *et al* revisited the dynamics in the $^1B_2(^1\Sigma_u^+)$ state using sub-20 fs 198 nm pump and 159 nm probe pulses described in section 2 [7]. As shown in figure 14, the broad

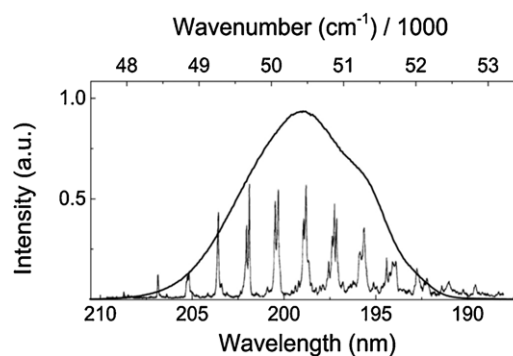


Figure 14. Photoabsorption spectrum of CS_2 showing sharp vibrational progressions (reprinted with permission from [45]. © 1983 American Institute of Physics) and the broad spectrum of our pump pulse.

198 nm pump pulse covers almost entire $^1B_2(^1\Sigma_u^+)$ – $^1A_1(^1\Sigma_g^+)$ photoabsorption spectrum of CS_2 and creates a spatially confined initial wave packet. Figure 15 compares the two time–energy maps of photoelectron spectra measured using (b) the 198 nm pump and 264 nm probe pulses and (c) the 198 nm pump and 159 nm probe pulses. The latter exhibits very clear oscillatory motions of vibrational wave packet. The signal at 4 eV corresponds to photoionization from the linear geometry of CS_2 while the signal at around 1.3 eV is from the turning point at the bent structure. Observation of such clear wave packet dynamics was not possible with longer pulse durations and longer probe wavelength employed in previous studies. As schematically shown in figure 15(a), the CS_2^+ cation is linear, so that high photon energy is required for photoionization from the bent structure to vibrationally excited states of the cation.

3. Subpicosecond time-resolved x-ray absorption spectroscopy using a hard x-ray free electron laser

The orbital energies of inner-shell electrons largely vary with the atomic numbers, and their energies further exhibit ‘chemical shifts’ depending on the chemical bonds formed by the atoms. X-ray photoelectron spectroscopy enables measurements of these chemical shifts, so that x-ray photoelectron spectroscopy is also termed electron spectroscopy for chemical analysis [46, 47]. Another method to measure the chemical shift is x-ray absorption spectroscopy, in which the x-ray absorption intensity steeply increases when photon energy exceeds the electron binding energy. Furthermore, the absorption spectrum exhibits structures in the post-ionization region, which are useful for extracting geometrical structure around the electron-emitting atom. The spectral feature within ca. 50 eV from the edge, called XANES (x-ray absorption near edge structure), is due to shape resonance, transient electron trapping by a molecule. The structure far above the ionization threshold is called EXAFS (extended x-ray absorption fine structure), which is caused by quantum mechanical interference between an outgoing photoelectron wave and the scattered waves from adjacent atoms. From the oscillatory features in EXAFS, interatomic distances between the electron-emitting atom and adjacent

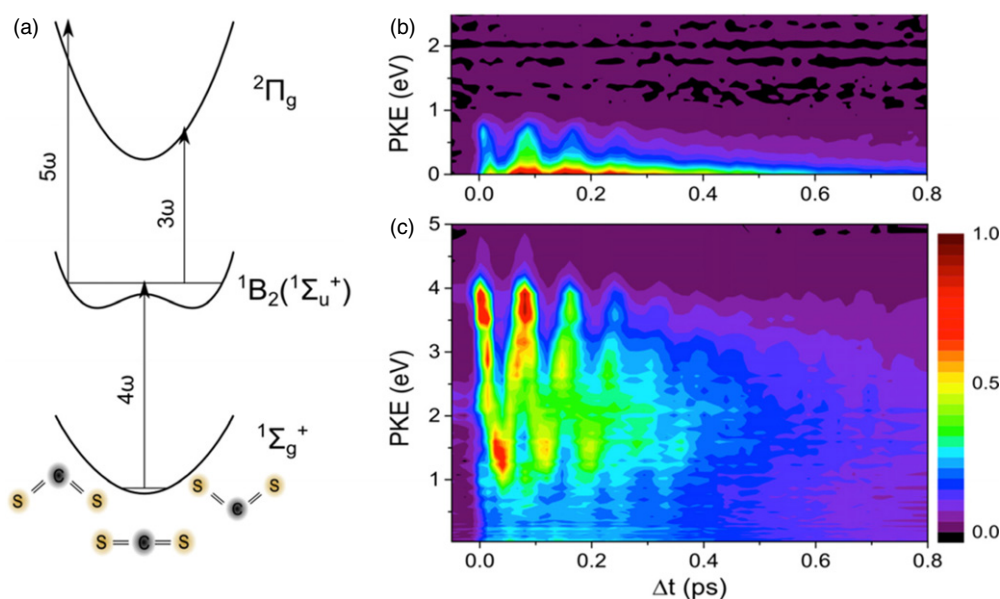


Figure 15. (a) Schematic potential energy diagram of CS_2 . Two-dimensional (2D) map of photoelectron kinetic energy (PKE) distributions as a function of the pump–probe delay time using (b) a 3ω probe pulse and (c) a 5ω probe pulse.

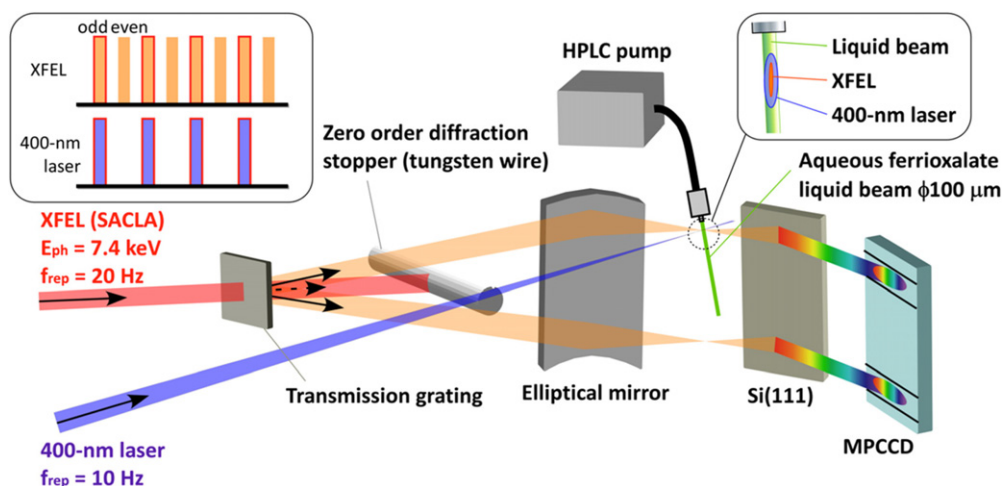


Figure 16. Experimental setup for the dual-beam dispersive detection method. Spatial overlap of the sample liquid beam, pump laser and x-ray is depicted in the upper right inset. Temporal sequence of 400 nm pump and x-ray probe pulses is shown in the upper left inset. Reprinted with permission from [15]. © 2014 The Optical Society of America.

atoms can be determined. With the element-specificity and structural information, time-resolved x-ray absorption spectroscopy (TRXAS) serves as a useful experimental method to probe the electronic and structural dynamics of materials. The ability of XAS to probe the local structure is, in some sense, similar to resonance Raman spectroscopy employed for studying local structures of macromolecules. Readers interested in general principle of TRXAS, particularly with liquid targets, can refer to excellent review articles published previously [48–52].

When synchrotron radiation is employed, the time resolution of TRXAS is tens of picoseconds. The time resolution can be improved by using a time-slicing technique, which extracts a femtosecond x-ray pulse using interaction of a femtosecond visible laser pulse with an electron bunch in a storage ring [53, 54]. However, the time-slicing

technique inevitably sacrifices photon flux and produces only 10–100 photons/pulse. XFELs offer considerably higher photon fluxes of more than 10^{10} photons/pulse and are opening a new avenue for TRXAS. XFEL-based TRXAS has already been implemented at LCLS and SACLA. At LCLS, TRXAS was performed by fluorescence detection, in which x-ray fluorescence from the target was monitored while scanning the x-ray photon energy [55]. At SACLA, direct absorption spectroscopy was performed using a broadband x-ray radiation and x-ray polychromator [15, 56]. The advantage of XFEL-based TRXAS is its high time-resolution; note, however, that the actual time resolution is limited to several hundred fs to 1 ps owing to timing jitter of the XFEL, even if the x-ray pulse duration is as short as tens of fs. The disadvantage of XFEL-based TRXAS is a low duty cycle, which is restricted by the repetition rate of XFEL, currently 120 Hz at LCLS and

30 Hz at SACLA. These repetition rates are contrasted with kHz (fs pulses) to MHz (ps pulses) repetition rates of TRXAS at synchrotron radiation facilities, which are limited by the repetition rates of synchronous lasers [57, 58]. Because of a high-repetition rate and stability, TRXAS using synchrotron radiation can be applied to dilute solutions at concentration levels down to mM; XFEL-based TRXAS requires tens of mM. The XFEL-based TRXAS also has the limitation of a fixed beam time, because the XFEL is a linear accelerator and only a few experiments can be performed at one time.

At LCLS, Lemke *et al* have studied photoinduced dynamics of spin crossover in the iron (II) tris(2,2'-bipyridine) complex in water using a 400 nm pulse and hard x-ray radiation (ca. 7.1 keV at the K-edge of Fe) [55]. The timing jitter between the pump and probe pulses was estimated to be 160 fs for time scans while between 300 and 500 fs in spectral scans. The TRXAS experiment at SACLA has been performed under similar conditions [15].

Figure 16 shows the experimental setup employed at SACLA [15]. The x-ray radiation from SACLA is split using a transmission grating. The zero-order (undiffracted) x-ray beam is blocked, and the +1 (upper) and -1 (lower) order x-rays are employed as the signal and reference beams, respectively. Each of these beams has a pulse energy of 1.4 μJ (1.2×10^9 photon/pulse at 7.12 keV). Two beams are focused using a single elliptical mirror, in which only the signal beam intersects with a sample liquid jet at the focal point while the reference beam does not. The spot size of the signal beam on the sample is 250 μm (vertical) by 25 μm (horizontal). The polychromator consists of an ultra-precisely figured elliptical mirror, a diffraction grating of a flat silicon (1 1 1) crystal, and a multi-port charge-coupled device (MPCCD) detector [20]. The signal and reference spectra are recorded simultaneously with the MPCCD for each XFEL shot to extract the absorption spectrum. The MPCCD has a pixel size of $50 \times 50 \mu\text{m}^2$, an imaging area of $25.6 \times 51.2 \text{mm}^2$, and a quantum efficiency of ca. 0.6 at 7 keV. The spectral range of the spectrometer is 67 eV, which is wider than the XFEL bandwidth. The spectral resolution of the polychromator is ca. 1 eV. The photon numbers incident to each pixel of MPCCD is ca. 7×10^2 . A single x-ray photon creates 2,000 electron-hole pairs while the system noise is about 300; therefore, the MPCCD enables single photon counting. The 400 nm light is the second harmonic of a Ti:sapphire laser with a homemade double-pass power amplifier added to a commercial regenerative amplifier. The 400 nm pump pulse has a time duration of 100 fs (fwhm), pulse energy of 1.1 mJ, and the spot size is 400 μm (vertical) by 100 μm (horizontal) which is larger than the spot size of the x-ray probe pulse at the sample. The fluence of 400 nm laser is 3.5J cm^{-2} on the sample. The 400 nm pump and x-ray probe beams are crossed at the sample with a small angle of less than 10° . The cross-correlation including the timing jitter is about 200 fs; while the time zero gradually drifts less than 1 ps for integration times of many hours. The labelling of individual pulses and sorting of the signals for each pump-probe delay will improve the time-resolution. The 400 nm pulse illuminates the sample synchronously with every other x-ray pulse. Therefore, the transient absorption signal is

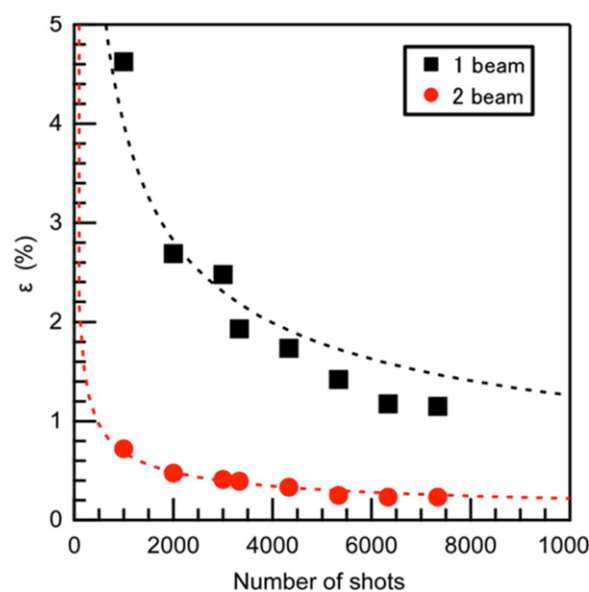


Figure 17. The minimum detectable absorbance using single-beam detection (black squares) and dual-beam detection (red circles).

extracted as the difference between the absorption spectra for even and odd-numbered x-ray pulses. Owing to the stochastic nature of the SASE-XFEL, the single-shot spectrum of XFEL has a spiky structure and the spectrum also fluctuates on a shot-to-shot basis. The difference spectrum extracted by the dual beam method eliminates the spiky structure and integration over 500 shots smooth out the spectral fluctuation. Figure 17 shows the minimum absorbance detectable using only a single reference beam (black square) or dual beams (red circle) in the pump-probe experiment plotted as a function of the number of pump-probe pulse pairs. With the single beam method, the minimum detectable absorbance does not reach 1% even after 6000 pulse pairs, while the dual beam method achieves well below 1% at 1000 pulse pairs. Thus, it is effective to use the dual beam method to detect a small transient absorption signal.

Femtosecond TRXAS was performed for aqueous 0.5 M ammonium iron(III) oxalate trihydrate solution. Rentzepis and coworkers [59, 60] have previously studied photochemistry of a ferrioxalate complex using TRXAS with a laser-plasma x-ray source; however, the detailed dynamics have not been understood yet. We employed this system for the first feasibility test of our TRXAS using SACLA. The sample was discharged into air from a fused silica capillary with a 100 μm inner diameter and at a flow rate of 5mL min^{-1} . The liquid beam was a cylindrical shape, and its speed was 10.6m s^{-1} . The sample concentration was selected to make the optical density for x-ray radiation reasonably high; the molar extinction coefficient ϵ at the K-edge of iron (7.1 keV) is $22.8 \text{cm}^{-1} \text{M}^{-1}$ and the absorbance for aqueous 0.5 M solution is about 0.1. For observing the pump-probe signal, we need to photoexcite a large fraction of molecules in the observation region with the pump pulse. The number of iron complexes in the volume illuminated by x-ray is estimated as 1.5×10^{14} . Since the molar extinction coefficient at 400 nm is $160 \text{cm}^{-1} \text{M}^{-1}$ [13], photon numbers of more than 8.8×10^{13} are required for pumping half of these complexes to

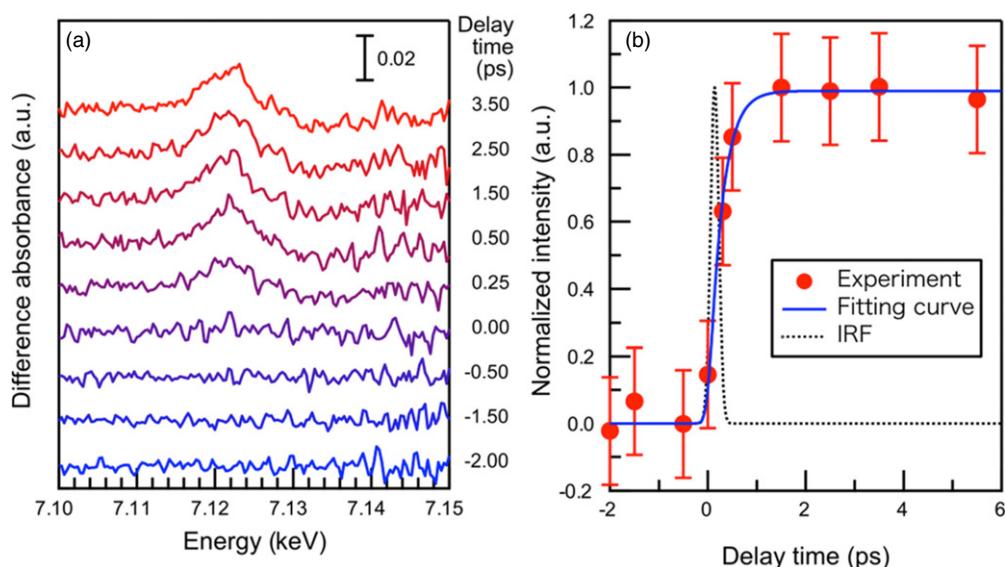


Figure 18. (a) Time-resolved difference x-ray absorption spectra of aqueous 0.5 M ammonium iron(III) oxalate trihydrate solution. (b) Temporal dependence of the absorbance change at 7.120 ± 0.004 keV in the difference absorption spectra. The instrumental response function is shown in the dotted line, and the solid blue curve is least-squares fitting assuming a single exponential rise. Reprinted with permission from [15]. © 2014 The Optical Society of America.

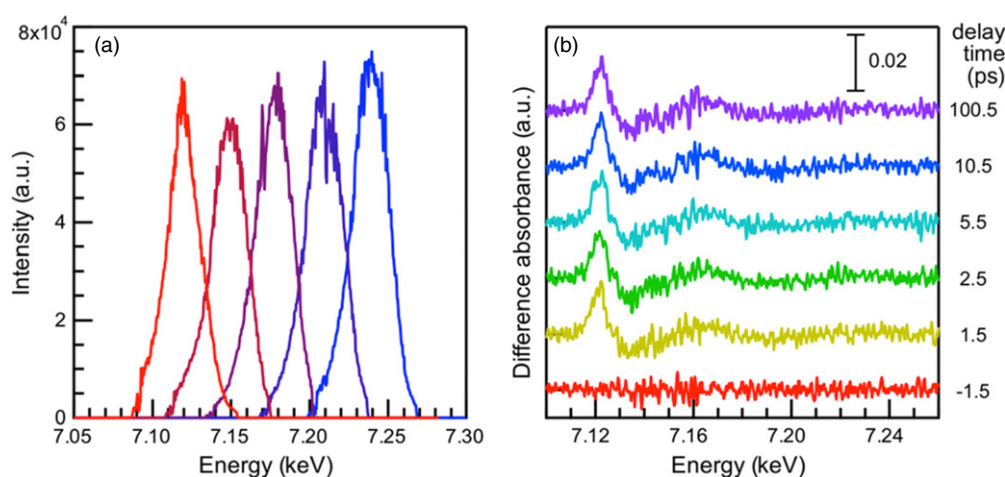


Figure 19. (a) Five different XFEL spectra employed to measure the transient absorption spectra for 7.10–7.26 keV. Each spectrum is the average over 20 000 shots. (b) Time-resolved difference absorption spectra. Each spectrum is constructed from five spectra of different energy regions. Reprinted with permission from [15]. © 2014 The Optical Society of America.

the excited state. In terms of laser pulse energies this is $44 \mu\text{J pulse}^{-1}$. Since the pump laser spot size is 6.4 times larger than the x-ray beam, the pump pulse energy should be at least $280 \mu\text{J pulse}^{-1}$. Thus, we employed a rather intense pump pulse (1.1 mJ). A fresh sample solution kept in a container covered with aluminium foil was used for measurements; the sample solution was not circulated to avoid buildup of the concentration of photodissociated products. The liquid flow rate and hydrodynamic stabilities were continuously monitored using a high performance liquid chromatography pump and a CCD camera, respectively. Entire experiments were performed at room temperature and under atmospheric pressure.

Figure 18(a) shows the difference x-ray absorption spectra of the $[\text{Fe}(\text{C}_2\text{O}_4)_3]^{3-}$ complex around the K-edge of the Fe atom measured using the multiplex scheme at several pump-

probe time delays. A positive absorbance change indicates an increased absorption by 400 nm photoexcitation. The peak position appearing at 7.12 eV is lower than the K-edge of the steady-state spectrum of the molecule. The shape of the difference spectra does not vary with the time delay. Figure 18(b) shows the temporal dependence of the absorbance change at 7.120 ± 0.004 keV. Assuming an instrumental response time of 200 fs expected from timing jitter of the x-ray pulse and the duration of the 400 nm pulse, the least-squares fitting of the experimental data provides a rise time of 260 ± 50 fs as shown in solid line.

Figures 19(a) and (b) present the x-ray pulse and difference absorption spectra for wider energy regions, respectively. We employed five different central photon energies, as shown in different colours in figure 19(a), by changing the undulator setting to observe the energy

region of 7.10–7.26 keV. The difference spectra merged from five spectra taken for different energy regions are shown in figure 19(b) at six time delays. The spectral profile is essentially the same even at a time delay of 100 ps. Our result indicates that the transient species has a rather similar geometrical structure with the ground state complex and its lifetime is longer than 100 ps. With the limited experimental evidences from the first TRXAS using SACLA, the assignment of this transient species has not been made. Further information such as transient infrared absorption spectra, the lifetime measurements and kinetic analysis will be of assistance for elucidating its chemical nature. However, the result clearly demonstrates impressive performance of ultrafast TRXAS using SACLA. The largest absorbance change seen in figure 19(b) is 0.02, whereas the rms of the fluctuation in absorbance change is 0.002. The absorbance change of 0.02 corresponds to variation of the arriving x-ray photon numbers by 35 photons/pulse, so that the fluctuation of 0.002 is equivalent to 3.5 photons. Note that the system noise per energy bin (10 pixels of MPCCD) is about 3.5×10^3 electrons, corresponding to 1.75 photons. Thus, the system noise of the detector is an important factor for the minimal detection limit using this method.

4. Summary and outlook

For elucidating chemical reaction mechanisms of polyatomic molecules, it is essential to understand electronic dynamics, including non-adiabatic transitions, which induce nuclear dynamics in a molecule. Vacuum ultraviolet radiation generated by filamentation four-wave mixing or high harmonic generation is useful for observation of valence electrons in combination with photoelectron spectroscopy. When the probe photon energy exceeds the electron binding energy of a molecule, all energetically possible electronic deactivation processes can be observed including internal conversion down to the ground state. On the other hand, such high-energy probe photons will directly ionize the ground state molecules, so that detection of the pump–probe signal becomes difficult. This is also the case in x-ray absorption spectroscopy. X-ray radiation is indispensable for probing inner-valence and inner-shell electrons and detecting the chemical shifts of their binding energies and the changes of post-ionization spectral features; however, the ground state molecules dominate the x-ray absorption, so that the absorption spectra of photoexcited species must be extracted from the difference spectrum (with and without the pump pulse). This usually requires independent evaluation of the excitation efficiency using the pump pulse. The pump–probe spectroscopy using short wavelength radiation often requires complementary basic information from the transient absorption or photoelectron spectroscopies performed with visible and ultraviolet radiation in the laboratories.

A stable light source with a high-repetition rate will be advantageous for spectroscopic purposes, especially of dense targets such as liquids, even if the pulse energies are limited. From this viewpoint, light sources with repetition rates of 1 kHz or higher are attractive. Construction of a kHz

free electron laser is technically and financially challenging; however, it is underway in Europe. Steering of kHz electron beams into different beam lines will reduce the drawback of the current free electron laser facilities by enabling several experiments performed at the same time. The energy recovery linac is one of other possibilities for future x-ray light sources. Observation of pre-edge absorption features and the extended x-ray absorption fine structure requires high sensitivity and stability of the spectrometer, especially when high time-resolution is pursued.

Both TRPES and TRXAS provide limited information on nuclear dynamics in polyatomic molecules, which occur with 3 N-6 degrees of freedom (nonlinear molecules). Furthermore, ultrafast electronic dynamics in solution undergo concurrently with intra and intermolecular vibrational relaxation, so that the spectrum of the same electronic state can change as a function of time. Spectral analysis including vibrational cooling is quite challenging. Mixed quantum/classical molecular dynamics (QM/MM) simulations will assist interpretation of such complex experimental results.

Each of the advanced light sources based on a tabletop laser, a linear accelerator and a storage ring has different advantages, and it is effective to make the best combination of experimental measurements using different light sources to solve a complex problem.

Acknowledgments

I express my gratitude to my group members, especially Yoshi-ichi Suzuki, Takuya Horio, Zuo Peng, Roman Spesyvtsev and Yoshihiro Ogi for their essential contribution to the studies described in this article. I am also grateful to Vlasta Bonacic-Koutechy and Roland Mitric for theoretical supports for TRPEI, and Yuki Obara, Kazuhiko Misawa, Tetsuo Katayama and Makina Yabashi and all members at SACLA for the joint project on TRXAS.

References

- [1] Agostini P and DiMauro L F 2004 *Rep. Prog. Phys.* **67** 1563
- [2] Niikura H and Corkum P B 2007 *Adv. At. Mol. Opt. Phys.* **54** 511
- [3] Krausz F and Ivanov M 2009 *Rev. Mod. Phys.* **81** 163
- [4] Takahashi E J, Lan P, Mucke O D, Nabekawa Y and Midorikawa K 2013 *Nature Commun.* **4** 2691
- [5] Fuji T, Horio T and Suzuki T 2007 *Opt. Lett.* **32** 2481
- [6] Fuji T, Suzuki T, Serebryannikov E E and Zheltikov A 2009 *Phys. Rev. A* **80** 063822
- [7] Horio T, Spesyvtsev R and Suzuki T 2013 *Opt. Express* **21** 22423
- [8] Chin S L 2010 *Femtosecond Laser Filamentation* (New York: Springer)
- [9] Ackermann W *et al* 2007 *Nature Photon.* **1** 336
- [10] Emma P *et al* 2010 *Nature Photon.* **4** 641
- [11] Shintake T *et al* 2008 *Nature Photon.* **2** 555
- [12] Ishikawa T *et al* 2012 *Nature Photon.* **6** 540
- [13] Hara T *et al* 2013 *Phys. Rev. Spec. Top.- Accel. Beams* **16** 080701
- [14] Yabashi M *et al* 2013 *J. Phys. B: At. Mol. Opt. Phys.* **46** 164001
- [15] Obara Y *et al* 2014 *Opt. Express* **22** 1105
- [16] Zuo P, Fuji T and Suzuki T 2010 *Opt. Express* **18** 16183

- [17] Chandler D W and Houston P L 1987 *J. Chem. Phys.* **87** 1445
- [18] Eppink A T J B and Parker D H 1997 *Rev. Sci. Instrum.* **68** 3477
- [19] Suzuki T 2012 *Int. Rev. Phys. Chem.* **31** 265
- [20] Garcia G A, Nahon L and Powis I 2004 *Rev. Sci. Instrum.* **75** 4989
- [21] Zuo P, Fuji T, Horio T, Adachi S and Suzuki T 2012 *Appl. Phys. B* **108** 815
- [22] Ghotbi M, Beutler M and Noack F 2010 *Opt. Lett.* **35** 3492
- [23] Beutler M, Ghotbi M and Noack F 2011 *Opt. Lett.* **36** 3726
- [24] Schneider R and Domcke W 1988 *Chem. Phys. Lett.* **150** 235
- [25] Suzuki Y I, Fuji T, Horio T and Suzuki T 2010 *J. Chem. Phys.* **132** 174302
- [26] Fuji T, Suzuki Y I, Horio T, Suzuki T, Mitric R, Werner U and Bonacic-Koutecky V 2010 *J. Chem. Phys.* **133** 234303
- [27] Horio T, Fuji T, Suzuki Y I and Suzuki T 2009 *J. Am. Chem. Soc.* **131** 10392
- [28] Suzuki Y-I and Suzuki T 2012 *J. Chem. Phys.* **137** 194314
- [29] Wang L, Kohguchi H and Suzuki T 1999 *Faraday Discuss.* **113** 37
- [30] Stert V, Farmanara P and Radloff W 2000 *J. Chem. Phys.* **112** 4460
- [31] Liu S Y *et al* 2010 *Phys. Rev. A* **81** 031403
- [32] Humeniuk A, Wohlgemuth M, Suzuki T and Mitric R 2013 *J. Chem. Phys.* **139** 134104
- [33] Gromov E V, Trofimov A B, Vitkovskaya N M, Schirmer J and Koppel H 2003 *J. Chem. Phys.* **119** 737
- [34] Gromov E V, Trofimov A B, Vitkovskaya N M, Koppel H, Schirmer J, Meyer H D and Cederbaum L S 2004 *J. Chem. Phys.* **121** 4585
- [35] Lucchese R R, Takatsuka K and Mckoy V 1986 *Phys. Rep.* **131** 147
- [36] Arasaki Y, Takatsuka K, Wang K and McKoy V 2010 *J. Chem. Phys.* **132** 124307
- [37] Gavrilov N, Salzmann S and Marian C M 2008 *Chem. Phys.* **349** 269
- [38] Farmanara P, Stert V and Radloff W 1999 *J. Chem. Phys.* **111** 5338
- [39] Hertel I V and Radloff W 2006 *Rep. Prog. Phys.* **69** 1897
- [40] Townsend D, Satzger H, Ejdrup T, Lee A M D, Stapelfeldt H and Stolow A 2006 *J. Chem. Phys.* **125** 234302
- [41] Bisgaard C Z, Clarkin O J, Wu G R, Lee A M D, Gessner O, Hayden C C and Stolow A 2009 *Science* **323** 1464
- [42] Hockett F D, Wallace K D, Schmieder A H, Caruthers S D, Pham C T N, Wickline S A and Lanza G M 2011 *IEEE Trans. Med. Imaging* **30** 22
- [43] Hockett P, Bisgaard C Z, Clarkin O J and Stolow A 2011 *Nature Phys.* **7** 612
- [44] Fuji T, Suzuki Y I, Horio T and Suzuki T 2011 *Chem.-An Asian J.* **6** 3028
- [45] Hemley R J, Leopold D G, Roebber J L and Vaida V 1983 *J. Chem. Phys.* **79** 5219
- [46] Hufner S 2003 *Photoelectron Spectroscopy: Principles and Applications* (Berlin: Springer)
- [47] Barr T L 1994 *Modern ESCA: the Principles and Practice of X-Ray Photoelectron Spectroscopy* (Boca Raton, FL: CRC Press)
- [48] Chen L X 2005 *Annu. Rev. Phys. Chem.* **56** 221
- [49] Bressler C and Chergui M 2010 *Annu. Rev. Phys. Chem.* **61** 263
- [50] Chergui M 2010 *Acta Crystallogr. A* **66** 229
- [51] Chen L X and Zhang X 2013 *J. Phys. Chem. Lett.* **4** 4000
- [52] Penfold T J, Milne C J and Chergui M 2013 *Advances in Chemical Physics* vol 153 ed S A Rice and A R Dinner (New York: Wiley)
- [53] Schoenlein R W, Chattopadhyay S, Chong H H W, Glover T E, Heimann P A, Shank C V, Zholents A A and Zolotarev M S 2000 *Science* **287** 2237
- [54] Beaud P *et al* 2007 *Phys. Rev. Lett.* **99** 174801
- [55] Lemke H T *et al* 2013 *J. Phys. Chem. A* **117** 735
- [56] Katayama T *et al* 2013 *Appl. Phys. Lett.* **103** 131105
- [57] Lima F A *et al* 2011 *Rev. Sci. Instrum.* **82** 063111
- [58] Haldrup K *et al* 2012 *J. Phys. Chem. A* **116** 9878
- [59] Chen J, Zhang H, Tomov I V, Wolfsherg M, Ding X L and Rentzepis P M 2007 *J. Phys. Chem. A* **111** 9326
- [60] Chen W K, Chen J and Rentzepis P M 2013 *J. Phys. Chem. B* **117** 4332